SCIENCE CHINA PRESS

SCIENCE CHINA Chemistry
https://doi.org/10.1007/s11426-025-2899-1

ARTICLES

Heptacyclic spiro-TADF emitters with efficient long-wavelength emission via through-space interactions

Sheng-Yi Yang[1†], Zi-Qi Feng[2†], Cheng Liu[1†], Jianyu Zhang[1], Zihao Deng[1], Kai Zhang[3], Fan-Cheng Kong[5], Philip C. Y. Chow[5], Ryan T. K. Kwok[1], Zuo-Quan Jiang[2*], Jacky W. Y. Lam[1*], Liang-Sheng Liao[2,3*] & Ben Zhong Tang[1,4*]

[1]Department of Chemistry, Hong Kong Branch of Chinese National Engineering Research Center for Tissue Restoration and Reconstruction, The Hong Kong University of Science and Technology, Hong Kong 999077, China
[2]Institute of Functional Nano & Soft Materials (FUNSOM), Jiangsu Key Laboratory for Carbon-Based Functional Materials & Devices, Soochow University, Suzhou 215123, China
[3]Macao Institute of Materials Science and Engineering, Macau University of Science and Technology, Macao 999078, China
[4]School of Science and Engineering, Shenzhen Institute of Aggregate Science and Technology, The Chinese University of Hong Kong, Shenzhen (CUHK-Shenzhen), Shenzhen 518172, China
[5]Department of Mechanical Engineering, The University of Hong Kong, Hong Kong 999077, China
†Equally contributed to this work.
*Corresponding authors (email: zqjiang@suda.edu.cn; chjacky@ust.hk; lsliao@suda.edu.cn; tangbenz@cuhk.edu.cn)

Received 26 May 2025; Accepted 15 July 2025; Published online 22 October 2025

Abstract Efficient thermally activated delayed fluorescence (TADF) emitters can be developed using intramolecular through-space charge transfer (TSCT) in spiro compounds featuring a donor-σ-acceptor (D-σ-A) configuration. However, traditional TSCT TADF molecules often struggle with weak charge transfer, making long-wavelength emission challenging. In this study, a series of efficient TSCT TADF molecules with curved structures was synthesized by incorporating heptacyclic spiro structures with various donors. Although the spiro-carbon atom disrupts through-bond conjugation, the curved molecular configuration enhances intramolecular through-space interactions. These interactions, including intramolecular carbon-carbon and hydrogen-involved interactions, increase molecular rigidity and boost photoluminescence quantum yield up to 98%. The robust intramolecular TSCT allows precise tuning of long-wavelength emissions from yellow to red (556–647 nm) in dilute toluene solutions. Organic light-emitting diodes (OLEDs) based on these molecules exhibit efficient long-wavelength electroluminescence from yellow-green to red (544–626 nm), achieving a maximum external quantum efficiency of up to 22.1%. This represents the first TSCT TADF system with D-σ-A configuration capable of producing yellow, orange, and red electroluminescence, offering new strategies for developing efficient red and near-infrared TSCT TADF emitters.

Keywords heptacyclic spiro structure, thermally activated delayed fluorescence, through-space interactions, organic light-emitting diodes, emission-tunable

1 Introduction

Luminescent molecules/polymers based on non-conjugated structures find it challenging to achieve long-wavelength emission and precise tuning of emission wavelengths due to the interruption of electron delocalization along the bonds [1–5]. So far, some non-conjugated polymers can achieve full-spectrum emission under external stimuli (such as pressure, temperature, excitation wavelength) or by introducing specific end groups and heteroatoms, which alter the polymer conformation and enhance intramolecular/intermolecular through-space conjugation (TSC) [4,6–9]. However, the luminescent properties of these polymers are inevitably affected by impurities or unknown structures, making precise control of their luminescence very difficult. Additionally, the reported non-conjugated polymers have low photoluminescence quantum yields (PLQY) and low exciton utilization efficiency, greatly limiting their application in the field of organic electroluminescence [2,4,5].

In the field of non-conjugated luminescent small molecules, thermally activated delayed fluorescence (TADF) molecules with spiro structures based on intramolecular TSC and/or through-space charge transfer (TSCT) have developed rapidly in recent years due to their unique molecular structure, excellent bipolar transport properties, and high thermal stability [10–24]. In such molecules, the inherent sp^3 hybridized spiro-carbon atoms can effectively separate the electron clouds of the molecular frontier orbitals, thereby achieving efficient TADF properties. So far, scientists have developed several types of efficient spiro-type TSCT TADF emitters (Figure 1). For orthogonal spiro TSCT TADF molecules with a hexacyclic spiro structure, the spiro-carbon atom disrupts intramolecular through-bond conjugation (TBC) and through-bond charge transfer (TBCT). The inherent spiro conjugation, cross conjugation and homoconjugation within the molecule confer efficient emission. By rationally selecting molecular scaffolds, donors (D), acceptors (A), and adjusting the D/A arrangement within the molecule, constructed TADF molecules can achieve high PLQY and high exciton utilization (Figure 1a, b). However, due to the inherently weak TSCT, the emission wavelengths of these molecules are currently concentrated in the deep blue, blue, and green regions, making it challenging to precisely control efficient long-wavelength emission by altering the D/A structure, and even constructing TSCT TADF molecules with multiple π-stacked structures [10–34].

In this work, a series of efficient TSCT TADF molecules was constructed by introducing heptacyclic spiro structures with different donors to form curved structures, which provides strong intramolecular through-space interactions (Figure 1c). The abun-

Citation: Yang SY, Feng ZQ, Liu C, Zhang J, Deng Z, Zhang K, Kong FC, Chow PCY, Kwok RTK, Jiang ZQ, Lam JWY, Liao LS, Tang BZ. Heptacyclic spiro-TADF emitters with efficient long-wavelength emission via through-space interactions. *Sci China Chem*, https://doi.org/10.1007/s11426-025-2899-1

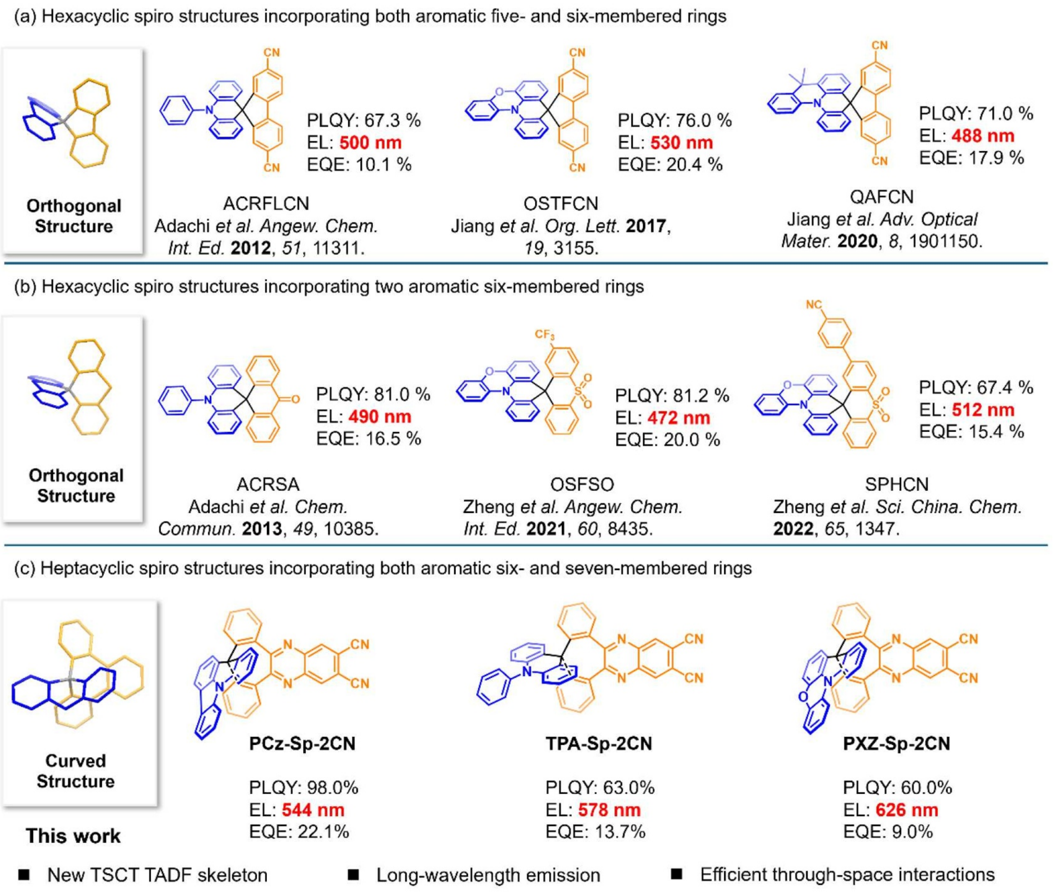

Figure 1 (Color online) Representative TSCT TADF emitters based on spiro compounds featuring a D-σ-A configuration. (a) Hexacyclic spiro structures incorporating both aromatic five- and six-membered rings. (b) Hexacyclic spiro structures incorporating two aromatic six-membered rings. (c) Heptacyclic spiro structures incorporating both aromatic six- and seven-membered rings.

dant intramolecular interactions enhance molecular rigidity and effectively suppress non-radiative transitions, ensuring high emission efficiency [1,3,25,35]. Moreover, the efficient intramolecular TSCT properties enable precise tunable long-wavelength emissions. For instance, these molecules achieve yellow (**PCz-Sp-2CN**, 556 nm), orange (**TPA-Sp-2CN**, 607 nm), and red (**PXZ-Sp-2CN**, 647 nm) emissions in dilute toluene solutions, and achieved high PLQY of 98%, 63%, and 60% in doped films, respectively. Furthermore, when applied as emitters in organic light emitting diodes (OLEDs), they achieved efficient electroluminescence (EL) with yellow-green (**PCz-Sp-2CN**, 544 nm), orange (**TPA-Sp-2CN**, 578 nm), and red (**PXZ-Sp-2CN**, 626 nm) emissions. The maximum external quantum efficiency (EQE) values reached as high as 22.1%. This is the first reported TSCT TADF system with D-σ-A configuration capable of achieving yellow, orange, and red electroluminescence. More importantly, this is the first reported heptacyclic spiro TADF system with D-σ-A configuration, and its device performance ranks among the highest based on spiro TADF molecules with D-σ-A configuration. This work provides a suitable model for a deeper understanding of the TSCT effect in spiro-type molecules and offers a practical design strategy for developing efficient TSCT-type full-spectrum (blue to near red) luminescent materials [21,36–46].

2 Results and discussion

2.1 Synthesis and characterization

As shown in Scheme 1, the synthesis of the target products involves the following steps. First, 2-bromo triarylamine derivatives (compounds **1**, **2**, and **3**) undergo lithium-halogen exchange reactions with *n*-butyllithium (*n*-BuLi) at low temperature (−78 °C), forming the corresponding triarylamine lithium intermediates. Subsequently, these intermediates undergo nucleophilic addition reactions with 5*H*-dibenzo[a,d] [7] annulen-5-one to yield the corresponding tertiary alcohol derivatives. Then, under acidic conditions, the tertiary alcohol derivatives undergo Friedel-Crafts alkylation to produce the corresponding heptacyclic spiro intermediates (**4**, **5**, and **6**, white solids, yields > 81%) [47]. Following this, the heptacyclic spiro intermediates are oxidized by benzeneseleninic anhydride to generate heptacyclic spiro diketone derivatives **7** (light yellow powder, 28%), **8** (yellow powder, 23%), and **9** (yellow powder, 29%) [48–50]. Finally, the heptacyclic spiro diketone derivatives undergo addition-condensation reactions with 4,5-diaminophthalonitrile to obtain the target products **PCz-Sp-2CN** (yellow powder, 94%), **TPA-Sp-2CN** (orange powder, 90%), and **PXZ-Sp-2CN** (dark red powder, 93%). It is noteworthy that all the spiro-molecules exhibit unique curved molecular structures (detailed structures can be seen in the single crystal section), primarily due to the highly twisted molecular configuration of the heptacyclic spiro diketone derivatives (such as intermediate **9**, CCDC: 2435146). The curved molecular configuration results in strong intramolecular through-space interactions, enabling precise tunable long-wavelength emissions [35]. To further analyze the impact of the heptacyclic spiro structure on the photophysical properties of the molecules, we also synthesized a control molecule **2CN** through the addition-condensation reaction of benzil with 4,5-diaminophthalonitrile. The final products were characterized by

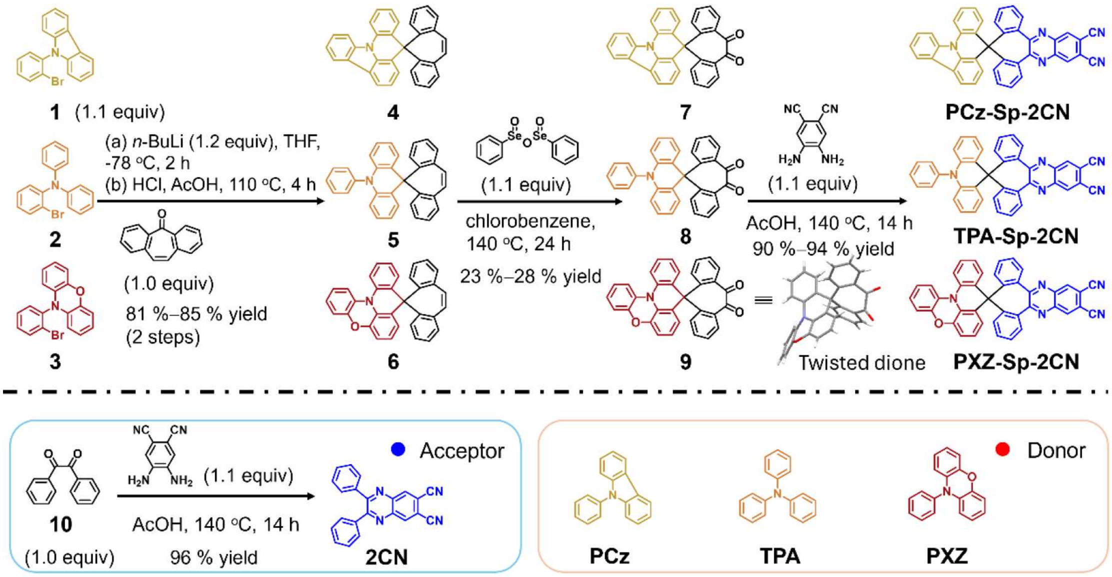

Scheme 1 (Color online) Synthetic routes to **2CN**, **PCz-Sp-2CN**, **TPA-Sp-2CN**, and **PXZ-Sp-2CN**.

nuclear magnetic resonance (^{1}H and ^{13}C NMR), high-resolution mass spectrometry, and single-crystal diffraction. For details, please see the Supporting Information online.

2.2 Single crystals

The single crystals involved in this work were obtained by solvent diffusion at room temperature; for more information, see Tables S1–S5 (Supporting Information online). As shown in Figure 2, for **2CN**, **PCz-Sp-2CN**, **TPA-Sp-2CN**, and **PXZ-Sp-2CN**, the electron acceptor unit (quinoxaline-6,7-dinitrile, QDCN) exhibits a classic large planar configuration, which facilitates face-to-face stacking and significant π-π interactions between molecules. In contrast, the donor of these molecules shows notable differences. For **2CN**, due to steric effects, the dihedral angles between the planes of the two benzene rings connected to the QDCN unit and the plane of the QDCN unit are quite large, with θ_1 and θ_2 reaching 40.02° and 49.93°, respectively. For the curved spiro-molecules, the anchoring effect of the spiro-structure and abundant intramolecular through-space interactions (C–H···π, C–H···heteroatoms) significantly reduce these dihedral angles (θ_3–θ_6: 29.19° to 37.72°). Notably, for **PXZ-Sp-2CN**, the more twisted structure of the phenoxazine containing heptacyclic spiro-structure results in θ_7 being 46.25°, which is noticeably prominent than the others (Figure 2a). Thus, by rationally designing the molecular structure, precise control over steric effects and intramolecular through-space interactions can be achieved. Additionally, due to the rigidifying effect of the spiro structure, the planarity between the QDCN unit and the connected phenyl rings in the spiro molecule is better compared to **2CN**. This could also be one of the reasons for the redshift in the emission of spiro molecules.

The single-crystal structures reveal that the molecular structures of the heptacyclic spiro compounds are distinctly different from traditional pentacyclic spiro-structures featuring two aromatic five-membered rings (such as spirobifluorene, SBF) and hexacyclic spiro-structures incorporating two aromatic six-membered rings or both aromatic five- and six-membered rings (such as 10-phenyl-10*H*-spiro[acridine-9,9′-xanthene] (SAX) and 10-phenyl-10*H*-spiro[acridine-9,9′-fluorene]) [51]. In the heptacyclic spiro-structures, the spiro-carbon atom is not coplanar with the other six carbon atoms, resulting in curved molecular configurations for **PCz-Sp-2CN**, **TPA-Sp-2CN**, and **PXZ-Sp-2CN** [48–50,52]. Compared to the orthogonal configurations of SBF or SAX spiro compounds, this curved molecular structure leads to efficient intramolecular through-space interactions, such as intramolecular carbon-carbon interactions (ICCI) and intramolecular hydron-involved interactions (IHII), which are intertwined to form the through-space interactions. As shown in Figure 2, the numbers of ICCI (n_{ICCI}) in **PCz-Sp-2CN**, **TPA-Sp-2CN**, and **PXZ-Sp-2CN** are 27, 22, and 29, respectively, and their IHII numbers (n_{IHII}) are 18, 19, and 22, respectively. These numerous intramolecular interactions not only enhance molecular rigidity and reduce non-radiative transitions in the excited state but also provide a bridge for intramolecular TSC and TSCT properties, laying the foundation for precise control of long-wavelength emission [35].

Furthermore, as shown in Figure 2c, the introduction of the heptacyclic spiro-structure greatly affects intermolecular interactions and molecular stacking. For **2CN**, strong intermolecular π-π interactions ($d_{\pi\text{-}\pi}$: 3.347–3.398 Å) and D-A interactions ($d_{\mathrm{D\text{-}A}}$: 3.137–3.383 Å) exist between molecules, resulting in antiparallel stacking. These strong intermolecular π-π interactions cause a significant redshift in the solid-state (powder) emission of **2CN**, details of which will be discussed in the photophysical section. In contrast, for **PCz-Sp-2CN** and **TPA-Sp-2CN**, the introduction of the bulky heptacyclic spiro-structure significantly weakens intermolecular interactions, with almost no π-π interactions ($d_{\pi\text{-}\pi} >$ 3.5 Å), which is beneficial for high-efficiency emission. Particularly, for **PXZ-Sp-2CN**, the intermolecular D-A distance ($d_{\mathrm{D\text{-}A}}$: 3.092–3.358 Å) is smaller than the previous three, attributed to the stronger electron-donating ability of the phenoxazine unit. Like **2CN**, it also has strong π-π interactions ($d_{\pi\text{-}\pi}$: 3.371–3.398 Å), leading to significant redshift in solid-state (powder) emission. Interestingly, in these heptacyclic spiro emitters, despite the spiro-carbon atom interrupting the through-bond conjugation, the more efficient intramolecular through-space interactions provide effects like traditional through-bond conjugation, achieving precise tunable emission wavelengths across the almost full spectrum [25,26,53].

2.3 Photophysical properties

The molecular photophysical properties significantly rely on the

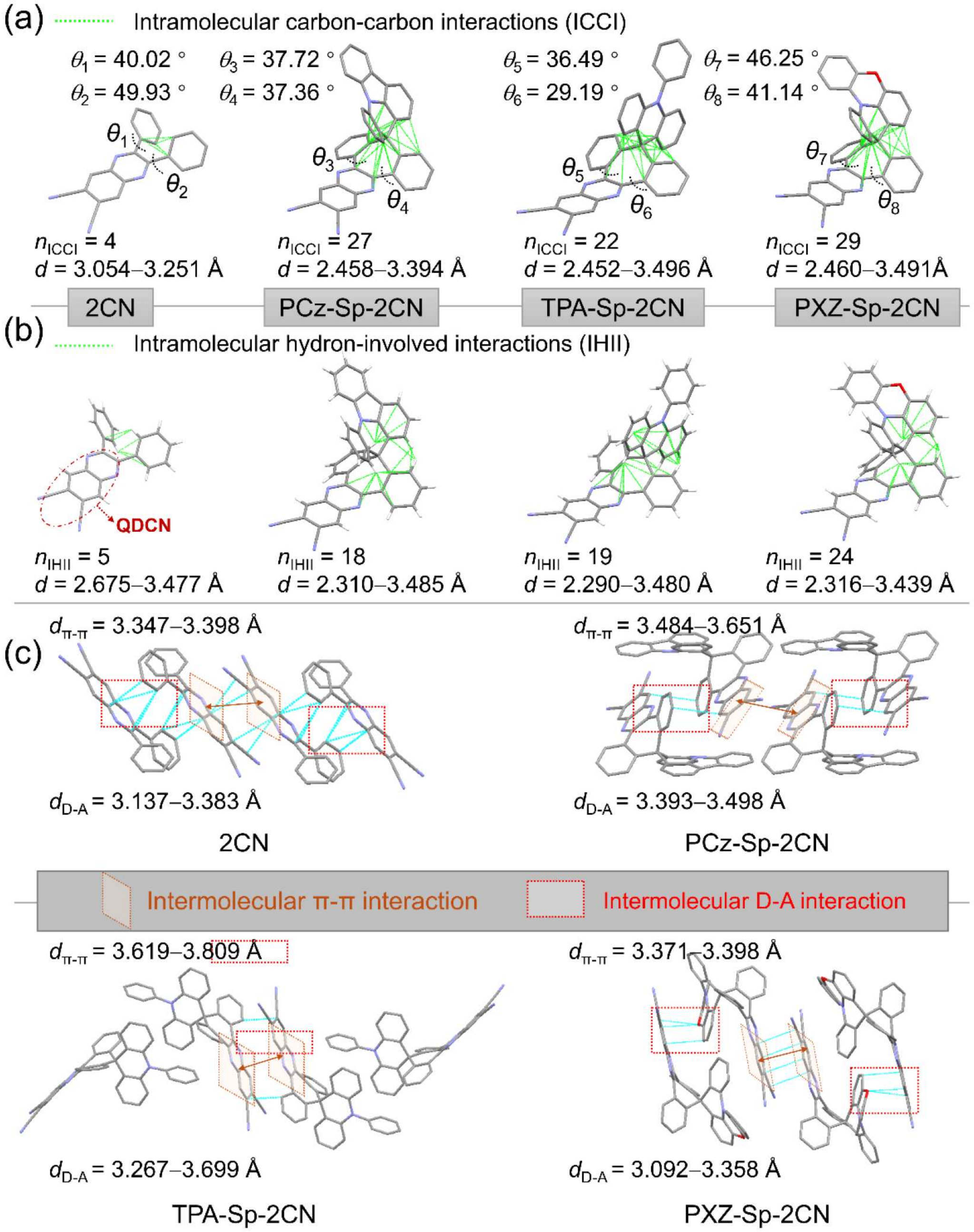

Figure 2 (Color online) Intramolecular/intermolecular interactions of **2CN**, **PCz-Sp-2CN**, **TPA-Sp-2CN**, and **PXZ-Sp-2CN** in the crystalline phase. (a) Number of intramolecular carbon-carbon interactions (n_{ICCI}) and (b) number of intramolecular hydron-involved interactions (n_{IHII}) of **2CN**, **PCz-Sp-2CN**, **TPA-Sp-2CN**, and **PXZ-Sp-2CN** in the crystalline phase. (c) Intermolecular interactions of **2CN**, **PCz-Sp-2CN**, **TPA-Sp-2CN**, and **PXZ-Sp-2CN** in the crystalline phase.

molecular structure. As mentioned above, the steric effects of different heptacyclic spiro donors can influence the molecular conformation, thereby affecting the intramolecular donor-acceptor through-space interactions. The photophysical properties of the molecules validate this viewpoint. As shown in Figure 3a, in dilute toluene solution (10^{-4} M), the ultraviolet-visible (UV-Vis) absorption spectra of **PCz-Sp-2CN**, **TPA-Sp-2CN**, and **PXZ-Sp-2CN**, which incorporate a heptacyclic spiro-structure, show a slight but noticeable redshift compared to **2CN**. The weak absorption of around 450–550 nm can be attributed to intramolecular TSCT absorption, which is similar to classical spirobifluorene TSCT-type molecules [25,26,28]. The intramolecular TSCT becomes more pronounced with increasing electron-donating ability of the donor, and **PXZ-Sp-2CN** exhibits a distinct intramolecular charge transfer absorption peak around 480 nm. Benefit from the introducing of the donors containing heptacyclic spiro-structure, the photoluminescence (PL) spectra of **PCz-Sp-2CN**, **TPA-Sp-2CN**, and **PXZ-Sp-2CN** in dilute toluene solutions display classic charge transfer peaks at 556 nm (yellow-green), 607 nm (orange), and 647 nm (red), respectively, representing redshifts of 126, 177, and 217 nm compared to **2CN** emitting at 430 nm. This work marks the first achievement of long-wavelength coverage of emission spectra through intramolecular TSCT, with detailed data in Table 1.

Further, we tested the low-temperature fluorescence and phosphorescence spectra of the molecules, as shown in Figure 3c, d. For **2CN**, the structured emission peaks between 400 and 470 nm match its room-temperature fluorescence emission peaks and are thus attributed to fluorescence emission, while the peaks

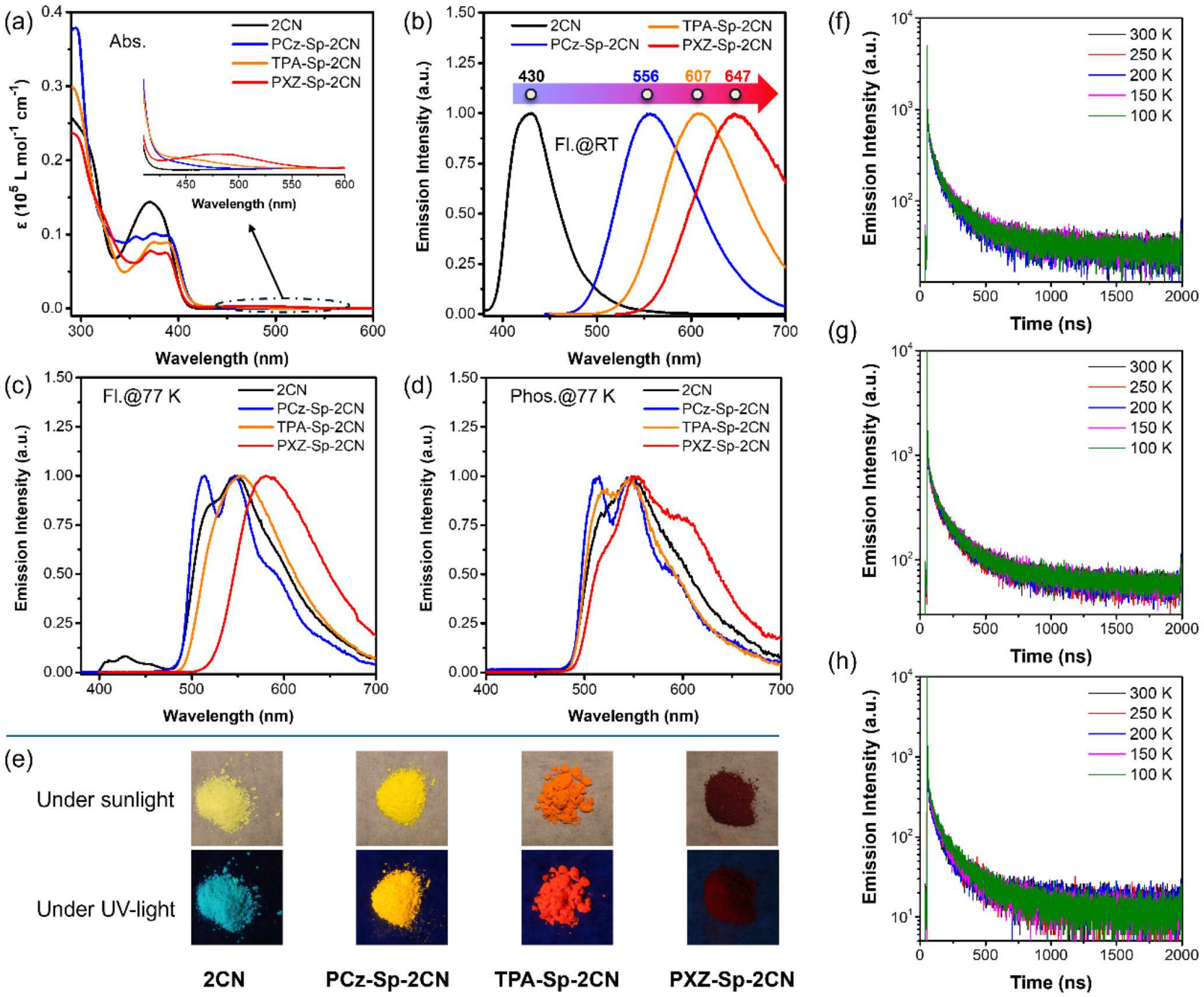

Figure 3 (Color online) The photophysical properties of **PCz-Sp-2CN**, **TPA-Sp-2CN**, and **PXZ-Sp-2CN**. (a) Absorption spectra and (b, c) fluorescence spectra measured at (b) room temperature and (c) 77 K; and (d) phosphorescence spectra of **2CN**, **PCz-Sp-2CN**, **TPA-Sp-2CN**, and **PXZ-Sp-2CN** in dilute toluene solutions (10^{-4} M); (e) photographs of samples taken under sunlight and under UV light excitation; transient PL characteristics of (f) **PCz-Sp-2CN**, (g) **TPA-Sp-2CN**, and (h) **PXZ-Sp-2CN** doped CBP films under nitrogen atmosphere.

Table 1 Photophysical properties of **2CN**, **PCz-Sp-2CN**, **TPA-Sp-2CN**, and **PXZ-Sp-2CN**

Compound	λ_{abs} (nm) [a)]	λ_{em} (nm) [a)]	PLQY (%) [b)]	τ_P (ns) [b)]	τ_D (ns) [b)]
2CN	371	430	–	–	–
PCz-Sp-2CN	356, 374, 386	556	98	31.2	186.4
TPA-Sp-2CN	376, 387	607	63	34.6	222.0
PXZ-Sp-2CN	372, 386, 483	647	60	8.2	127.9

a) In toluene solution (10^{-4} M) at room temperature. b) Measured in doped into 4,4′-bis(*N*-carbazolyl)-1,1′-biphenyl (CBP) host with 3 wt% (100 nm) under nitrogen atmosphere. τ_P (the prompt lifetime) and τ_D (the delayed lifetime) were obtained from the transient PL decay of doped films.

beyond 500 nm match its phosphorescence spectrum, indicating phosphorescence emission. Based on low-temperature fluorescence and phosphorescence spectra, the singlet-triplet energy gap (ΔE_{ST}) of **2CN** is 0.533 eV. Notably, the low-temperature fluorescence of **PCz-Sp-2CN**, **TPA-Sp-2CN**, and **PXZ-Sp-2CN** shows a significant blue shift compared to their room-temperature fluorescence, likely due to rigidochromic effects, commonly observed in metal complexes and TADF molecules [54,55]. Specifically, the low-temperature phosphorescence spectra of them further blue shift from their low-temperature fluorescence spectra. To further analyze this phenomenon, we tested the absorption, fluorescence, and phosphorescence spectra of molecular fragments (Figure S1, Supporting Information online), such as 9-phenyl-9*H*-carbazole (**PCz**), triphenylamine (**TPA**), and 10-phenyl-10*H*-phenoxazine (**PXZ**). Results indicate that **PCz-Sp-2CN**, **TPA-Sp-2CN**, and **PXZ-Sp-2CN** exhibit acceptor-related (QDCN) localized excited phosphorescence emission (Figure 3d). Meanwhile, we tested the room temperature fluorescence (Fl.@RT), low temperature fluorescence (Fl.@77 K), and low temperature phosphorescence (Phos.) of doped films of **PCz-Sp-2CN**, **TPA-Sp-2CN**, and **PXZ-Sp-2CN** (3 wt% doped in CBP, 100 nm). We found that their emission is similar to that in solution (Figure S2). It seems that due to inhibited molecular motion, **PCz-Sp-2CN**, **TPA-Sp-2CN**, and **PXZ-Sp-2CN** cannot form stable twisted intramolecular charge transfer triplet states (^{3}CT) at low temperatures, resulting in observable phosphorescence from the localized excited state of the acceptor fragment [30,55]. We have noticed that the triplet states of some "hot exciton" type luminescent materials can be obtained through sensitization strategies [56,57]. For TADF molecules, the Arrhenius activation energy (ΔE_a) values more effectively reflect the ΔE_{ST}. Thus, due to the difficulty in obtaining the ΔE_{ST} of the molecules through the fluorescence and phosphorescence spectra, we obtained their ΔE_a by testing the temperature-dependent spectra and temperature-dependent transient lifetimes (Figure S3) using the Arrhenius equation. The ΔE_a values for **PCz-Sp-2CN**, **TPA-Sp-2CN**, and **PXZ-Sp-2CN** are 2.3, 1.4, and 8.4 meV, respectively, indicating that all three have very small ΔE_{ST} values (Figure S4) [27,30].

It is evident from Figure 2c that there are significant donor-acceptor interactions between the molecules in crystals of **2CN**, **PCz-Sp-2CN**, **TPA-Sp-2CN**, and **PXZ-Sp-2CN**. Therefore, the solid-state (powder) emissions of these four molecules should exhibit a noticeable red shift compared to their solution. As shown in Figure S5, the emission peaks of these four compounds in solid state (powder) reached 477, 621, 646, and 699 nm, respectively. For **TPA-Sp-2CN**, its solid-state (powder) emission (646 nm) is red shifted by 39 nm compared to its emission in dilute toluene solution (607 nm). Since there is almost no π-π interaction between the molecules, this red shift in solid-state (powder) emission is attributed to intermolecular D/A interactions. In contrast, for **2CN**, **PCz-Sp-2CN**, and **PXZ-Sp-2CN**, due to the presence of some π-π interactions and strong intermolecular D/A interactions, their solid-state emissions (powder) are red-shifted by 47, 65, and 52 nm, respectively, compared to their solution emissions (Figure 3). Notably, the solid-state (powder) emission peak of **PXZ-Sp-2CN** reaches the near-infrared region (~700 nm). This phenomenon highlights the significant impact of intermolecular D/A interactions on solid-state emission, a factor often overlooked in previous studies of TSCT TADF molecules. Furthermore, we measured the PLQYs of **PCz-Sp-2CN**, **TPA-Sp-2CN**, and **PXZ-Sp-2CN** doped in CBP (3 wt%), which reached 98%, 63%, and 60%, respectively. The high PLQYs of these molecules are attributed to their efficient intramolecular through-space interactions and rigid molecular structures [53]. We note that the PLQY of **PCz-Sp-2CN** is significantly higher than that of **PXZ-Sp-2CN**. Like traditional D-(π)-A molecules, the energy gap law could significantly affect the emission efficiency. Temperature-dependent transient spectroscopy (Figure 3f–h) shows that **PCz-Sp-2CN**, **TPA-Sp-2CN**, and **PXZ-Sp-2CN** exhibit TADF properties, with delayed lifetimes of 186.4, 222.0, and 127.9 ns at room temperature, respectively (Table 1 and Table S6, Supporting Information online) [58,59]. These short delayed fluorescence lifetimes may be advantageous for subsequent OLED applications.

2.4 Theoretical calculations

To deeply analyze the relationship between molecular structure and optoelectronic properties, we performed density functional theory (DFT) and time-dependent DFT (TD-DFT) calculations on **2CN**, **PCz-Sp-2CN**, **TPA-Sp-2CN**, and **PXZ-Sp-2CN**. As shown in Figure 4, the highest occupied molecular orbital (HOMO) and the lowest unoccupied molecular orbital (LUMO) of **2CN** are distributed across the entire molecular framework, with a similar electron-hole distribution, indicating that its emission is from a locally excited state, consistent with its fluorescence emission. The ΔE_{ST} for **2CN** is 0.530 eV, aligning with its photophysical results (0.533 eV). In contrast, **PCz-Sp-2CN**, **TPA-Sp-2CN**, and **PXZ-Sp-2CN** have their HOMO localized on the donors and LUMO on the QDCN acceptor. The separation of HOMO-LUMO is facilitated by the spiro-carbon atom, resulting in very small ΔE_{ST} values of 0.082, 0.060, and 0.042 eV for **PCz-Sp-2CN**, **TPA-Sp-2CN**, and **PXZ-Sp-2CN**, respectively (Table S7). These small ΔE_{ST} values favor efficient TADF properties. We found that the oscillator strength (*f*) of the heptacyclic spiro TADF molecules is very small (< 0.06), like the spiro TSCT TADF molecules reported so far (Table S7). Moreover, the electron-hole distribution in **PCz-Sp-2CN**, **TPA-Sp-2CN**, and **PXZ-Sp-2CN** is separated between the donor and acceptor units, leading to efficient intramolecular TSCT [26]. These theoretical calculations are consistent with electrochemical results, showing that the LUMO of **PCz-Sp-2CN**, **TPA-Sp-2CN**, **PXZ-Sp-2CN**, and **2CN** are located on the acceptor units, resulting in minor LUMO energy level changes. However, the energy levels of HOMO, distributed on different donors, increase significantly with stronger electron-donating ability, reducing the energy gap and causing a substantial redshift in emission.

Interestingly, reduced density gradient (RDG) analysis (Figure 4c and Figure S6) shows significant intramolecular attractive interactions (green regions) between the donor and the acceptor fragments in **PCz-Sp-2CN**, **TPA-Sp-2CN**, and **PXZ-Sp-2CN** [26,27]. These interactions effectively restrict molecular vibrations, reducing non-radiative decay in the excited state. Further TD-DFT calculations confirm the electronic distribution, showing that the LUMO+5, LUMO+2, and LUMO+5 of **PCz-Sp-2CN**, **TPA-Sp-2CN**, and **PXZ-Sp-2CN**, respectively, are derived from spatial orbital overlap between donor and acceptor units, demonstrating efficient intramolecular TSCT characteristics (Figures S7–S9). Additionally, calculations of hole and electron distribution in full space reveal that the overlap between electrons and holes (S_m) in **2CN** (S_m = 0.271) is nearly ten times that of **PCz-Sp-2CN** (S_m = 0.023), **TPA-Sp-2CN** (S_m = 0.026), and **PXZ-Sp-2CN** (S_m = 0.020), indicating significant electron-hole separation in the latter three spiro-type molecules. Furthermore, the distance index (D_{index}) between hole and electron centroids shows much larger values for **PCz-Sp-2CN** (D_{index} = 6.599 Å), **TPA-Sp-2CN** (D_{index} = 5.772 Å), and **PXZ-Sp-2CN** (D_{index} = 6.132 Å) compared to **2CN** (D_{index} = 0.899 Å), indicating pronounced charge transfer excitation in spiro-type emitters. Similarly, the separation degree of holes and electrons (t_{index} = −1.001 Å) in **2CN** is less than 0, indicating no significant separation, whereas **PCz-Sp-2CN** (t_{index} = 4.418 Å), **TPA-Sp-2CN** (t_{index} = 3.769 Å), and **PXZ-Sp-2CN** (t_{index} = 4.209 Å) show significant separation, supporting strong intramolecular TSCT properties (Figure S10). These theoretical results align with photophysical properties, confirming that heptacyclic spiro molecules exhibit strong intramolecular TSCT properties, achieving precise control emission.

2.5 Thermal and electrochemical properties

We further analyzed the thermal stability of compounds **2CN**, **PCz-Sp-2CN**, **TPA-Sp-2CN**, and **PXZ-Sp-2CN**, with detailed data shown in Table 2. As illustrated, due to the smaller molecular weight of **2CN**, the differential scanning calorimetry (DSC) curve shows distinct temperature inflection points, with a glass transition temperature (T_g) of 76 °C, a crystallization temperature (T_c) of 126 °C, and a melting point (T_m) of 177 °C. When the donor containing heptacyclic spiro-structure is introduced, the increased molecular weight and strong intramolecular through-space interactions result in **PCz-Sp-2CN**, **TPA-Sp-2CN**, and **PXZ-Sp-2CN** exhibiting no obvious characteristic temperature inflection points within the tested temperature range (30–300 °C), indicating high morphological stability (Figure S11). According to the thermogravimetric analysis (TGA), the thermal decomposition temperature (T_d) of **2CN** is 279 °C, whereas **PCz-Sp-2CN**, **TPA-Sp-2CN**, and **PXZ-Sp-2CN** have T_d values of 362, 377, and 379 °C, respectively, further demonstrating their excellent thermal stability, which is beneficial for subsequent vacuum deposition and OLEDs fabrication

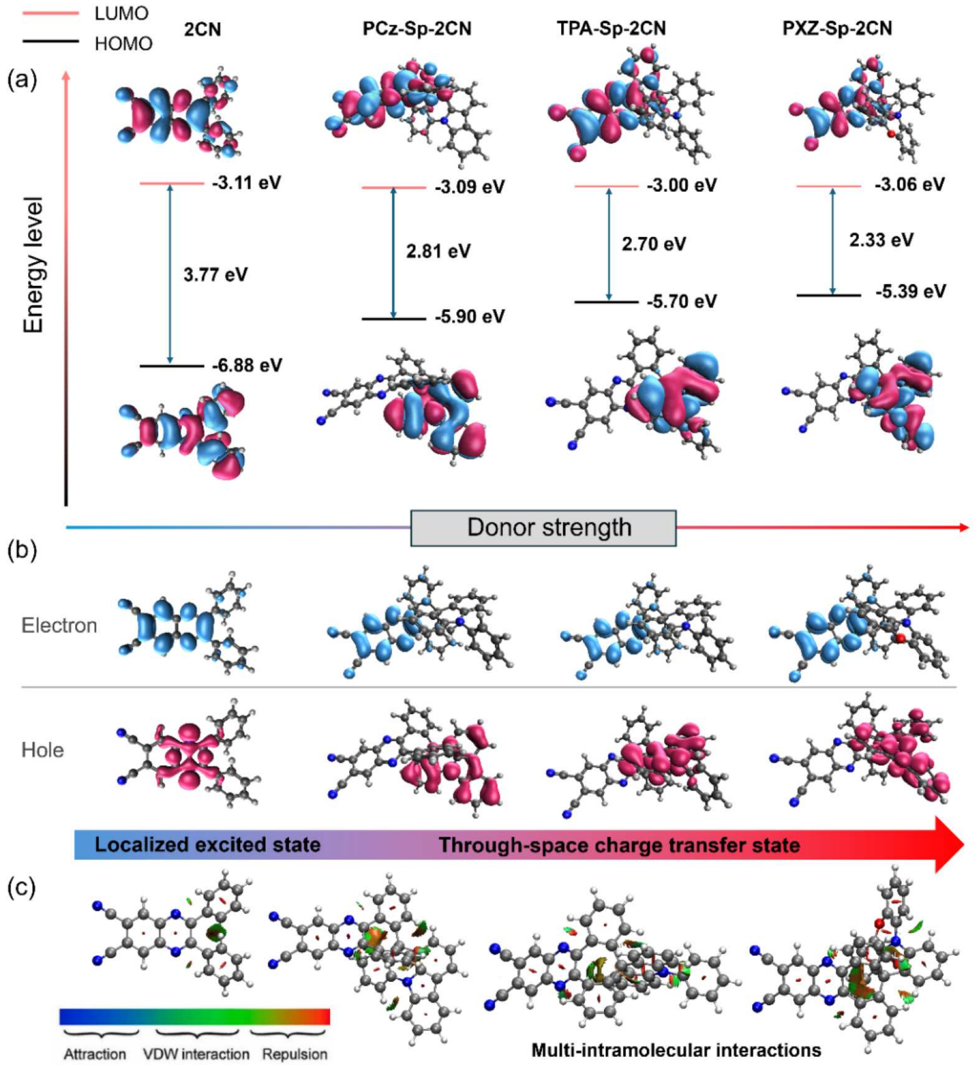

Figure 4 (Color online) Theoretical calculations. (a) HOMO and LUMO orbital distributions and calculated band gaps for **2CN**, **PCz-Sp-2CN**, **TPA-Sp-2CN**, and **PXZ-Sp-2CN** based on DFT at the B3LYP functional and 6-31G(d) basis set; (b) electron-hole analysis for **2CN**, **PCz-Sp-2CN**, **TPA-Sp-2CN**, and **PXZ-Sp-2CN** based on TD-DFT at the B3LYP functional and 6-31G(d) basis set; (c) reduced density gradient (RDG) *iso*-surfaces of **2CN**, **PCz-Sp-2CN**, **TPA-Sp-2CN**, and **PXZ-Sp-2CN**.

Table 2 Electrochemical and thermal parameters of **2CN**, **PCz-Sp-2CN**, **TPA-Sp-2CN**, and **PXZ-Sp-2CN**

Compound	E_{ox} (V) a)	E_{red} (V) a)	HOMO (eV)	LUMO (eV)	E_g (eV)	T_g/T_d (°C)
2CN	1.52	−0.81	−5.84	−3.51	2.33	76/279
PCz-Sp-2CN	1.32	−0.78	−5.64	−3.54	2.10	–/362
TPA-Sp-2CN	1.11	−0.77	−5.43	−3.55	1.88	–/377
PXZ-Sp-2CN	0.92	−0.79	−5.24	−3.53	1.71	–/379

a) In dichloromethane solution (in 5×10^{-3} M) using ferrocene as a reference.

(Figure S12).

Cyclic voltammetry (CV) tests indicate that the reduction potentials (E_{red}) of **2CN**, **PCz-Sp-2CN**, **TPA-Sp-2CN**, and **PXZ-Sp-2CN** are nearly identical, at −0.81, −0.78, −0.77, and −0.79 V, respectively, resulting in LUMO energy levels of −3.51, −3.54, −3.55, and −3.53 eV, respectively (Figure S13). The detailed data are shown in Table 2. This similarity reduction potential is due to the identical acceptor structure in all four molecules. In contrast, the different donor structures lead to significantly different oxidation potentials (E_{ox}), which decrease with increasing electron-donating ability, reaching 1.52, 1.32, 1.11, and 0.92 V, respectively. The corresponding HOMO energy levels are −5.84, −5.64, −5.43, and −5.24 eV. Suitable HOMO/LUMO energy levels facilitate electron and hole injection, transport, and recombination, laying the foundation for efficient electroluminescence [25]. Thus, thanks to the efficient intramolecular through-space interactions of heptacyclic spiro-type TSCT emitters, like traditional through-bond conjugated molecules, allow precise tuning of molecular energy levels and emission wavelengths by altering the donor/acceptor strength.

2.6 Electroluminescence properties

These heptacyclic spiro-structured TSCT TADF molecules exhibit excellent thermal stability, high PLQYs, and strong intramolecular through-space interactions, making them ideal for constructing efficient OLEDs [1,25–27]. As shown in Figure 5a, considering the energy level alignment of various functional layers in OLEDs, a multilayer device structure was employed to study their electroluminescent properties (Figure S14). The device structure is ndium tin ioxide (ITO)/HAT-CN (10 nm)/TAPC (40 nm)/TCTA (10 nm)/EML (20 nm)/B3PymPm (10 nm)/TmPyPB (45 nm)/Liq (2.5 nm)/Al (120 nm). In the emission layer (EML), **PCz-Sp-2CN**, **TPA-Sp-2CN**, and **PXZ-Sp-2CN** were doped into a CBP host at different concentrations. For the optimized device structure, 1,4,5,8,9,11-hexaazatriphenylenehexacarbonitrile (HAT-CN) and 8-hydroxyquinolinolato-lithium (Liq) serve as hole and electron injection layers, respectively, facilitating the injection of holes and electrons. 1,1-Bis[(di-4-tolylamino)phenyl]cyclohexane (TAPC) and tris(4-carbazoyl-9-ylphenyl)amine (TCTA), with excellent hole transport capabilities, are used as hole transport layers. Their HOMO levels, −5.5 and −5.8 eV respectively, match the energy levels of the hole injection layer and the emission layer, further promoting hole transport efficiency. To balance the hole/electron transport ability, 4,6-bis(3,5-di-3-pyridinylphenyl)-2-methylpyrimidine (B3PymPm), with a HOMO level of −6.9 eV, acts as a hole-blocking layer. 1,3,5-Tris(3-pyridyl-3-phenyl)benzene (TmPyPB) is used as an electron transport layer to facilitate electron injection and transport. This device structure design aims to achieve efficient OLEDs.

Specifically, as shown in Figure 5, OLEDs based on **PCz-Sp-2CN** achieved maximum current efficiency (CE), power efficiency (PE), and EQE of 50.0 cd A^{-1}, 45.9 lm W^{-1}, and 22.1%, respectively, with an EL peak at 544 nm at a 3 wt% doping ratio (Figure S15). Further leveraging strong intramolecular space interactions, OLEDs using **TPA-Sp-2CN** and **PXZ-Sp-2CN** as emitters showed EL peaks redshifted to 578 nm (orange) and 626 nm (red) under optimal doping conditions, while maintaining good device performance (Figures S16 and S17). Detailed data are shown in Table 3 and

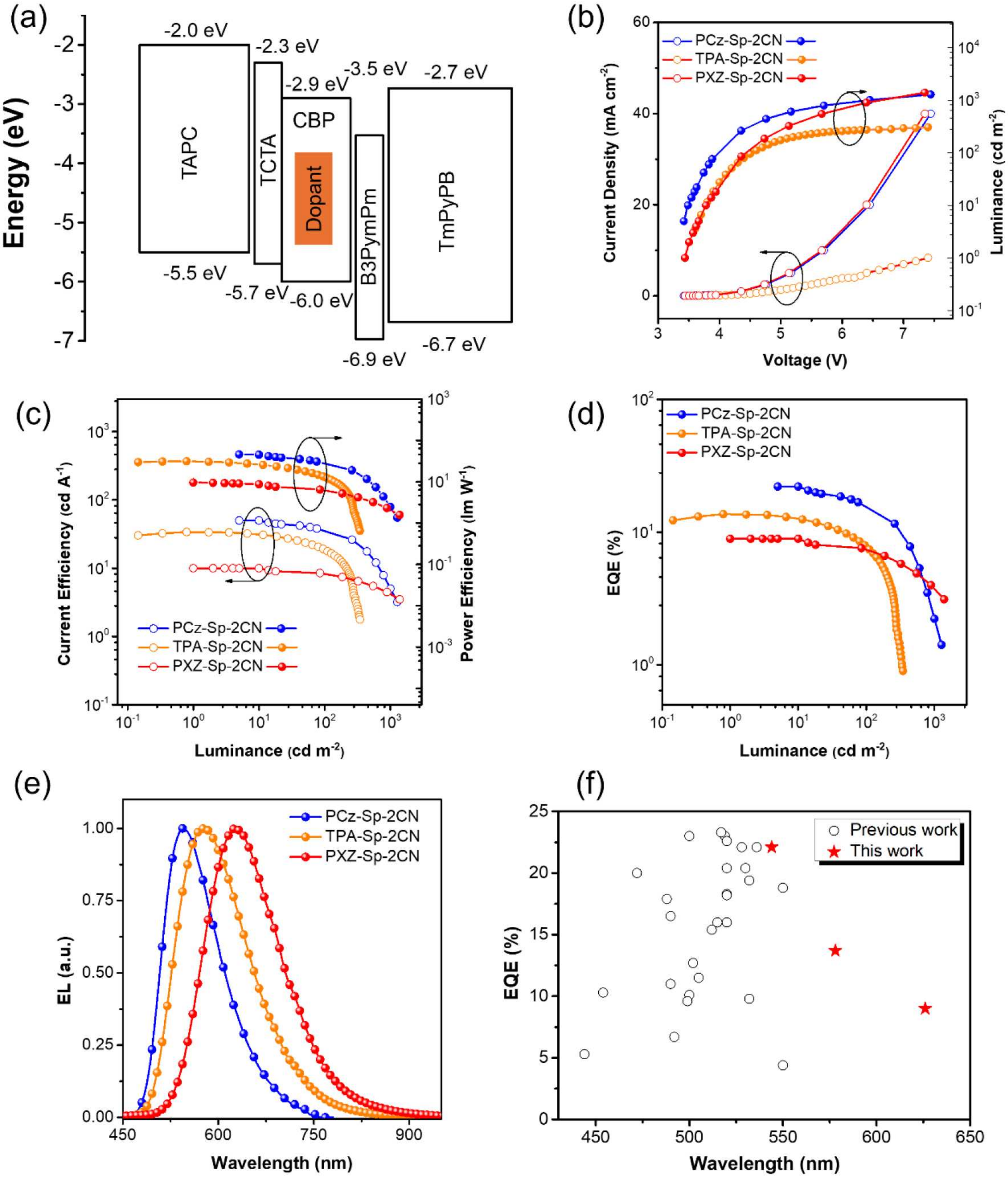

Figure 5 (Color online) The electroluminescent performance of **PCz-Sp-2CN**, **TPA-Sp-2CN**, and **PXZ-Sp-2CN**. (a) Device structure, (b) *J-V-L* characteristics, (c) CE-L-PE characteristics, (d) EQE-L characteristics, (e) EL spectra of **PCz-Sp-2CN**-, **TPA-Sp-2CN**-, and **PXZ-Sp-2CN**-doped devices. (f) Maximum EQE and the corresponding EL wavelength summary of spiro compounds featuring a D-σ-A configuration (hollow symbols). The red pentagrams are devices reported in this work.

Table 3 Electroluminescence characteristics of **PCz-Sp-2CN**, **TPA-Sp-2CN**, and **PXZ-Sp-2CN** doped devices at optimized dopant concentrations

Device	V $^{\text{a)}}$ (V)	CE $^{\text{b)}}$ (cd A^{-1})	PE $^{\text{b)}}$ (lm W^{-1})	EQE $^{\text{b)}}$ (%)	λ_{EL} $^{\text{c)}}$ (nm)	CIE (x, y)
PCz-Sp-2CN	3.42	50.0/35.1	45.9/27.6	22.1/15.5	544	0.41, 0.56
TPA-Sp-2CN	3.58	33.9/18.5	31.3/14.5	13.7/7.8	578	0.49, 0.50
PXZ-Sp-2CN	3.44	10.0/8.3	9.6/6.3	9.0/7.4	626	0.58, 0.41

a) Recorded at a luminance of 0.01 mA cm^{-2}. b) Maximum value, the value determined at the luminance of 100 cd m^{-2}. c) Determined from the EL spectra measured at a current density of 10 mA cm^{-2}.

Tables S8–S10. OLEDs based on **TPA-Sp-2CN** exhibited maximum CE, PE, and EQE of 33.9 cd A^{-1}, 31.3 lm W^{-1}, and 13.7%, respectively (Figure 5 and Figure S16). However, due to the energy gap law and the lower PLQY of **PXZ-Sp-2CN**, OLED performance based on **PXZ-Sp-2CN** decreased (EQE = 9.0%) (Figure 5 and Figure S17). Notably, this study is the first to achieve long spectral tuning and red emission for spiro compounds featuring a D-σ-A configuration (Figure 5f). Interestingly, as the doping rate increases, the operating voltage of all devices decreases, attributed to easier hole capture by the emitter at higher doping concentrations, leading to lower operating voltages, as shown in the current density-voltage-luminance (*J*-*V*-*L*) curves in Figure 5 [28,29]. Additionally, all devices display single EL emission peaks, indicating high energy transfer efficiency within the devices. To the best of our knowledge, this is the first reported TSCT TADF system capable of achieving yellow, orange, and red electroluminescence. Moreover, this work provides a suitable model for a deeper understanding of the TSCT effect in spiro-type molecules and offers a practical design strategy for developing efficient TSCT-type full-spectrum (blue to near red) luminescent materials [21,36–46,59]. Generally, however, the OLED performance of this work is not particularly ideal. In future work, we can select a more suitable host to construct more efficient OLEDs. Additionally, we can choose appropriate sensitizers in future work to further enhance device efficiency and suppress efficiency roll-off. Finally, the performance of non-doped devices based on **PCz-Sp-2CN**, **TPA-Sp-2CN**, and **PXZ-Sp-2CN** was investigated. As shown in Figure S18, the maximum EL peaks of **PCz-Sp-2CN**, **TPA-Sp-2CN**, and **PXZ-Sp-2CN** were bathochromically shifted to 680, 680 and 714 nm, respectively. Detailed data for the non-doped devices can be found in Table S11. This study also marks the first time achieving near red emission beyond the TSCT TADF series (Table S12).

3 Conclusions

In summary, this work constructed a series of efficient TSCT TADF molecules with curved structures by introducing heptacyclic spiro structures with different donors. Compared to the orthogonal or π-stacked configurations of spiro compounds, this curved molecular structure leads to efficient intramolecular through-space interactions. In dilute toluene solution, these molecules achieve yellow (**PCz-Sp-2CN**, 556 nm), orange (**TPA-Sp-2CN**, 607 nm), and red (**PXZ-Sp-2CN**, 647 nm) emissions. Furthermore, when used as emitters in OLEDs, they achieve efficient EL with yellow-green (**PCz-Sp-2CN**, 544 nm), orange (**TPA-Sp-2CN**, 578 nm), and red (**PXZ-Sp-2CN**, 626 nm) emissions, with maximum EQEs ranging from 9.0% to 22.1%. This is the reddest emission system for spiro-type TSCT TADF molecules reported so far. Furthermore, the non-doped OLEDs based on these emitters demonstrated deep red EL emission (**PCz-Sp-2CN** and **TPA-Sp-2CN** at 680 nm) and even near-infrared emission (**PXZ-Sp-2CN** at 714 nm). This work provides new insights and construction strategies for developing efficient TSCT TADF materials. Moreover, this work provides a suitable model for a deeper understanding of the TSCT effect in spiro-type molecules [60]. Future work could involve introducing stronger acceptors or donors to enhance intramolecular through-space interactions [61,62], aiming to construct more efficient deep-red and near-infrared TSCT TADF molecules and OLEDs.

Conflict of interest
The authors declare no conflict of interest.

Acknowledgement
This work was supported by the Research Grants Council of Hong Kong (16303221), the Innovation and Technology Commission of Hong Kong (ITC-CNERC14SC01), the Shenzhen Key Laboratory of Functional Aggregate Materials (ZDSYS20211021111400001), and the Science Technology Innovation Commission of Shenzhen Municipality (KQTD20210811090142053, JCYJ20220818103007014). The authors also acknowledge financial support from the National Natural Science Foundation of China (62175171, 62375193) and the Natural Science Foundation of Jiangsu Province (BK20221237). This work was also supported by the Suzhou Key Laboratory of Functional Nano & Soft Materials, Collaborative Innovation Center of Suzhou Nano Science & Technology (Nano-CIC), the 111 Project, and the Joint International Research Laboratory of Carbon-Based Functional Materials and Devices.

Funding note
Open access funding provided by Hong Kong University of Science and Technology.

Supporting information
The supporting information is available online at http://chem.scichina.com and http://link.springer.com/journal/11426. The supporting materials are published as submitted, without typesetting or editing. The responsibility for scientific accuracy and content remains entirely with the authors.

References

1 Yang SY, Qu YK, Liao LS, Jiang Z, Lee S. *Adv Mater*, 2022, 34: 2104125
2 Zhang H, Tang BZ. *JACS Au*, 2021, 1: 1805–1814
3 Zhang T, Xiao Y, Wang H, Kong S, Huang R, Ka-Man Au V, Yu T, Huang W. *Angew Chem Int Ed*, 2023, 62: e202301896
4 Shao S, Wang L. *Aggregate*, 2020, 1: 45–56
5 Liu B, Chu B, Zhu L, Zhang H, Yuan WZ, Zhao Z, Wan WM, Zhang XH. *Chin Chem Lett*, 2023, 34: 107909
6 Hu J, Li Q, Wang X, Shao S, Wang L, Jing X, Wang F. *Angew Chem Int Ed*, 2019, 58: 8405–8409
7 Chu B, Liu X, Li X, Zhang Z, Sun JZ, Yang Q, Liu B, Zhang H, Zhang C, Zhang XH. *J Am Chem Soc*, 2024, 146: 10889–10898
8 Liu X, Chu B, Xiong Z, Liu B, Tu W, Zhang Z, Zhang H, Sun JZ, Zhang X, Tang BZ. *Mater Horiz*, 2024, 11: 1579–1587
9 Chu B, Liu X, Xiong Z, Zhang Z, Liu B, Zhang C, Sun JZ, Yang Q, Zhang H, Tang BZ, Zhang XH. *Nat Commun*, 2024, 15: 366
10 Méhes G, Nomura H, Zhang Q, Nakagawa T, Adachi C. *Angew Chem Int Ed*, 2012, 51: 11311–11315
11 Nakagawa T, Ku SY, Wong KT, Adachi C. *Chem Commun*, 2012, 48: 9580–9582
12 Nasu K, Nakagawa T, Nomura H, Lin CJ, Cheng CH, Tseng MR, Yasuda T, Adachi C. *Chem Commun*, 2013, 49: 10385–10387
13 Ohkuma H, Nakagawa T, Shizu K, Yasuda T, Adachi C. *Chem Lett*, 2014, 43: 1017–1019
14 Wang YK, Wu SF, Yuan Y, Li SH, Fung MK, Liao LS, Jiang ZQ. *Org Lett*, 2017, 19: 3155–3158
15 Wang YK, Huang CC, Ye H, Zhong C, Khan A, Yang S, Fung M, Jiang Z, Adachi C, Liao L. *Adv Opt Mater*, 2020, 8: 1901150
16 Rao J, Zhao C, Wang Y, Bai K, Wang S, Ding J, Wang L. *ACS Omega*, 2019, 4: 1861–1867
17 Zhu XD, Peng CC, Kong FC, Yang SY, Li HC, Kumar S, Wang TT, Jiang ZQ, Liao LS. *J Mater Chem C*, 2020, 8: 8579–8584
18 Sharma N, Maciejczyk M, Hall D, Li W, Liégeois V, Beljonne D, Olivier Y, Robertson N, Samuel IDW, Zysman-Colman E. *ACS Appl Mater Interfaces*, 2021, 13: 44628–

44640
19 Zhang YP, Liang X, Luo XF, Song S, Li S, Wang Y, Mao Z, Xu W, Zheng Y, Zuo J, Pan Y. *Angew Chem Int Ed*, 2021, 60: 8435–8440
20 Yang D, Huh JS, Hong JI. *Dyes Pigments*, 2022, 197: 109837
21 Zhang YP, Song SQ, Mao MX, Li CH, Zheng YX, Zuo JL. *Sci China Chem*, 2022, 65: 1347–1355
22 Liao G, Lei J, Li S, Liu M, Qiao Y, Liu K, Wang N, Niu Q, Yin X. *Adv Opt Mater*, 2024, 12: 2301242
23 Khan A, Wang YK, Huang CC, Kumar S, Fung MK, Jiang ZQ, Liao LS. *Org Electron*, 2020, 77: 105520
24 Li X, Shi C, Mo Y, Rao J, Zhao L, Tian H, Sun N, Ding J. *J Mater Chem C*, 2022, 10: 4845–4850
25 Yang SY, Wang YK, Peng CC, Wu ZG, Yuan S, Yu YJ, Li H, Wang TT, Li HC, Zheng YX, Jiang ZQ, Liao LS. *J Am Chem Soc*, 2020, 142: 17756–17765
26 Yang SY, Feng ZQ, Fu Z, Zhang K, Chen S, Yu Y, Zou B, Wang K, Liao L, Jiang Z. *Angew Chem Int Ed*, 2022, 61: e202206861
27 Xie FM, Li HZ, Zhang K, Shen Y, Zhao X, Li Y, Tang J. *Angew Chem Int Ed*, 2022, 61: e202213823
28 Tang X, Cui LS, Li HC, Gillett AJ, Auras F, Qu YK, Zhong C, Jones STE, Jiang ZQ, Friend RH, Liao LS. *Nat Mater*, 2020, 19: 1332–1338
29 Peng CC, Yang SY, Li HC, Xie G, Cui L, Zou S, Poriel C, Jiang Z, Liao L. *Adv Mater*, 2020, 32: 2003885
30 Yu YJ, Song M, Meng XY, Qu YK, Wang XQ, Chen L, Yang SY, Zhou DY, Jiang ZQ, Liao LS. *Org Lett*, 2023, 25: 6024–6028
31 Li M, Hua L, Zhao J, Liu Y, Yan S, Ren Z. *Angew Chem Int Ed*, 2025, 64: e202501179
32 Poriel C, Rault-Berthelot J. *Acc Mater Res*, 2023, 4: 733–745
33 Jiang C, Miao J, Zhang D, Wen Z, Yang C, Li K. *Research*, 2022, 2022: 2022/9892802
34 Zhao Z, Zeng C, Peng X, Liu Y, Zhao H, Hua L, Su S, Yan S, Ren Z. *Angew Chem Int Ed*, 2022, 61: e202210864
35 Xu Q, Zhang J, Sun JZ, Zhang H, Tang BZ. *Nat Photon*, 2024, 18: 1185–1194
36 Ren H, Song Y, Yu R, Tian M, He L. *Dyes Pigments*, 2022, 204: 110389
37 Liu J, Feng Z, Peng C, Yu Y, Yang S, Jiang Z, Liao L. *Chin Chem Lett*, 2023, 34: 107634
38 Song Y, Tian M, Yu R, He L. *ACS Appl Mater Interfaces*, 2021, 13: 60269–60278
39 Song Y, Li Y, Yu R, Zhang K, He L. *Adv Opt Mater*, 2023, 11: 2300432
40 Wang Z, Li D, Li W, Zhang J, Luo M, Du S, Zhang X, Xu S, Ge Z. *Adv Opt Mater*, 2023, 11: 2300017
41 Li HZ, Xie FM, Zhang K, Shen Y, Zhou W, Li YQ, Wang WJ, Tang JX. *Chem Eng J*, 2022, 436: 135234
42 Huang T, Wang Q, Meng G, Duan L, Zhang D. *Angew Chem Int Ed*, 2022, 61: e202200059
43 Pei R, Lou J, Li G, Liu H, Yin X, Zhou C, Wang Z, Yang C. *Chem Eng J*, 2022, 437: 135222
44 Wu C, Liu W, Li K, Cheng G, Xiong J, Teng T, Che C, Yang C. *Angew Chem Int Ed*, 2021, 60: 3994–3998
45 Li Y, Song Y, Zhang K, Xiu Y, Wang P, Tian M, He L. *Dyes Pigments*, 2023, 219: 111572
46 Yu X, Cui D, Wang M, Wang Z, Wang M, Tu D, Bregadze V, Lu C, Zhao Q, Chen R, Yan H. *Chin Chem Lett*, 2025, 36: 110520
47 Brouillac C, Shen WS, Rault-Berthelot J, Jeannin O, Quinton C, Jiang ZQ, Poriel C. *Mater Chem Front*, 2022, 6: 1803–1813
48 Chen CT, Wei Y, Lin JS, Moturu MVRK, Chao WS, Tao YT, Chien CH. *J Am Chem Soc*, 2006, 128: 10992–10993
49 Chen CT, Tsai FY, Chiang CY, Chen CP. *J Phys Chem C*, 2017, 121: 15943–15948
50 Hung SF, Fang PH, Wei Y, Tsai FY, Chen CT, Kimura T, Samori S, Fujitsuka M, Majima T, Lin CH, Peng SH, Jou JH. *ACS Appl Mater Interfaces*, 2018, 10: 25561–25569
51 Chen Y, Xu J, Gao P. *Org Chem Front*, 2024, 11: 508–539
52 Chen Y, Yang SY, Ou X, Wang H, Kong FC, Chow PCY, Wang Y, Jiang Y, Zhao W, Sun J, Kwok RTK, Zheng DW, Yu W, Wang F, Lam JWY, Tang BZ. *J Am Chem Soc*, 2024, 146: 35462–35477
53 Yang SY, Wang J, Deng Z, Xu Y, Su X, Zhang L, Yang S, Kwok RTK, Lam JWY, Tang BZ. *Matter*, 2024, 7: 3390–3421
54 Tsuboyama A, Iwawaki H, Furugori M, Mukaide T, Kamatani J, Igawa S, Moriyama T, Miura S, Takiguchi T, Okada S, Hoshino M, Ueno K. *J Am Chem Soc*, 2003, 125: 12971–12979
55 Cui LS, Gillett AJ, Zhang SF, Ye H, Liu Y, Chen XK, Lin ZS, Evans EW, Myers WK, Ronson TK, Nakanotani H, Reineke S, Bredas JL, Adachi C, Friend RH. *Nat Photonics*, 2020, 14: 636–642
56 Xu Y, Liang X, Zhou X, Yuan P, Zhou J, Wang C, Li B, Hu D, Qiao X, Jiang X, Liu L, Su S, Ma D, Ma Y. *Adv Mater*, 2019, 31: 1807388
57 Xu Y, Xu P, Hu D, Ma Y. *Chem Soc Rev*, 2021, 50: 1030–1069
58 Zhang Q, Kuwabara H, Potscavage Jr. WJ, Huang S, Hatae Y, Shibata T, Adachi C. *J Am Chem Soc*, 2014, 136: 18070–18081
59 Yersin H, Czerwieniec R, Mataranga-Popa L, Mewes J, Cheng G, Che C, Saigo M, Kimura S, Miyata K, Onda K. *Adv Funct Mater*, 2022, 32: 2201772
60 Luo XF, Song SQ, Wu X, Yip C, Cai S, Zheng Y. *Aggregate*, 2024, 5: e445
61 Liang M, Liu L, Sun Y, Li J, Zhang L, Jiang X, Wu W. *Aggregate*, 2024, 5: e458
62 Huo Y, Qi H, He S, Li J, Song S, Lv J, Liu Y, Peng L, Ying S, Yan S. *Aggregate*, 2023, 4: e391